CHALMERS
UNIVERSITY OF TECHNOLOGY

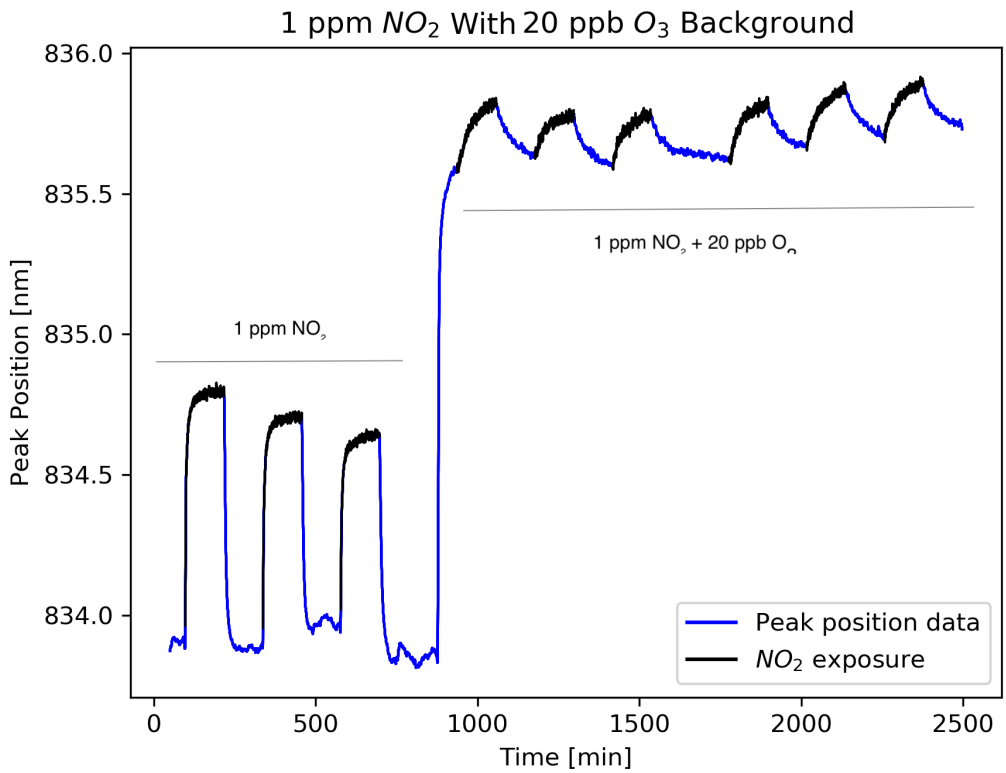

An Investigation Into the Effects of Ozone on a Nanoplasmonic Gas Sensor

Master's thesis in Applied Physics

Damien Pierce

Insplorion AB and The Department of Physics
CHALMERS UNIVERSITY OF TECHNOLOGY
Gothenburg, Sweden 2020

An Investigation Into the Effects of Ozone on a Nanoplasmonic Gas Sensor

Damien Pierce

Insplorion AB and The Department of Physics
Chalmers University of Technology
Gothenburg, Sweden 2020

An Investigation Into the Effects of Ozone on a Nanoplasmonic Gas Sensor
Damien Pierce

Supervisors: Dr Olof Andersson, Insplorion AB and Martin Sech, Insplorion AB
Examiner: Professor Christoph Langhammer, Department of Physics

Department of Physics
Chalmers University of Technology
SE-412 96 Gothenburg
Telephone +46 31 772 1000

Cover: Plot of the variation of peak position of a nanoplasmonic sensor with time, under the effect of 1 ppm NO_2 (first 3 exposures), and 1 ppm NO_2 with a constant 20 ppb O_3 background (last 6 exposures).

Typeset in LaTeX
Printed by Chalmers Reproservice
Gothenburg, Sweden 2020

An Investigation Into the Effects of Ozone on a Nanoplasmonic Gas Sensor
Damien Pierce
Insplorion AB and The Department of Physics
Chalmers University of Technology

Abstract

Gas sensing is critical to the continued good health and well-being of humankind. The sensing of NO_2 and O_3 are of particular importance, due to their negative effects on the respiratory system. Nanoplasmonic sensing is a relatively unexplored method that shows significant potential in gas detection. The nanoplasmonic sensor in this study has already been successful in detecting NO_2. However, its behaviour when exposed to O_3 has yet to be investigated. Using an experimental approach, it was found that the optimum temperature for O_3 sensing was 300°C, and 200°C for NO_2 sensing. The detection of 1 ppm NO_2 was possible with a constant 20 ppb O_3 background, for 2 hour long exposure times. The sensor response to O_3 showed rapid kinetics, with peak shifts of up to 2 nm, compared to 0.4 nm for NO_2, at the same concentration of 100 ppb. This thesis presents a starting point for a further study of nanoplasmonic sensor behaviour in the presence of these two harmful gases.

Keywords: Nanoplasmonics, Ozone, Nanotechnology, Sensing.

Acknowledgements

I would like to personally thank the whole of Insplorion AB for being so kind and welcoming. I especially would like to thank Martin Sech and Dr Olof Andersson for their support whenever questions arose. I am very grateful to Professor Christoph Langhammer for finding me this interesting project. Last but not least I would like to thank my girlfriend Sara Corinne Luren, and my parents, Lisa Cederholm & Daniel Pierce for their support throughout this entire endeavour.

Damien Pierce, Gothenburg, May 2020

Contents

List of Figures

1

Introduction

In Richard Feynman's 1959 lecture "There's Plenty of Room at the Bottom: An Invitation to Enter a New Field of Physics", the novel concept of nanophysics was introduced [1]. The properties of materials are vastly different at the nanoscale, creating opportunities for the development of useful applications [1]. In fact, the first use of nanoplasmonic effects can be traced back to the Bronze age, to create different colours in pottery when viewed at different angles [2].

The same properties of interest to the ancient civilizations can be used today in advanced sensing applications [3]. When incident light couples with the conduction electrons in metallic nanoparticles, causing oscillations, the oscillations exhibit resonance between certain wavelengths of light [3]. This creates pronounced observable effects in the extinction of the light by the nanoparticles, due to the higher adsorption/scattering efficiencies at the resonant wavelength [3]. Localised surface plasmons resonances are sensitive to the dielectric medium around them [3]. This creates the opportunity to employ metallic nanoparticles as precise, lightweight sensors with a rapid response time [4].

Gas sensing is of particular importance, especially recently with the rise in greenhouse gases [4]. Exposure to these gases leads to adverse health effects on the population in polluted areas [5]. Gases of interest include among others, NO_2 and O_3 [5][6]. Being able to reliably detect these gases would provide accurate real-time data of their concentration, improving the tracking of pollution levels [5].

Insplorion AB is currently developing a nanoplasmonic NO_2 sensor. This sensor is composed of gold nano discs with a metal oxide thin film coating. However, the effects of O_3 on the sensor remain to be determined. Understanding the adsorption and desorption characteristics of both O_3 and NO_2, as well as their effects when combined, are of key importance. This thesis aims to explore these interactions through experimentation.

2

Theory

2.1 The Need for Gas Sensors

The increased emission of greenhouse gases creates a need for reliable and precise sensing equipment [5]. Monitoring the increase of such gases is key to understanding the evolution of climate change [5]. Additionally, it is vital to keep track of air quality, to prevent any adverse health effects from spikes in pollution levels [5]. Of particular interest here are, NO_2 and O_3 [5][6]. Although O_3 is not a greenhouse gas, it is produced by reactions with greenhouse gases [6].

NO_2 is a toxic greenhouse gas, commonly regarded as the most harmful [5]. It has the lowest threshold limit value (TLV) of any greenhouse gas of 3 ppm [5]. The TLV is the concentration at which health is negatively impacted from continued exposure [5]. NO_2 is also known to contribute to an increase in ground level O_3, increasing smog [5]. NO_2 is produced to some degree by all combustion in atmospheric conditions [5]. It is corrosive and known to decrease immunity to respiratory diseases [5]. If it forms nitric acid, it can severely impact agricultural yields [5].

O_3 is present at ground level through three different processes [6]. Natural transport from the stratosphere, reactions from methane or biogenic organic volatiles with NO_x, and migration of O_3 from polluting sources [6]. The background concentration of O_3 varies during the year, with a maximum in spring [6]. This might be due to the increased solar radiation, acting on built up winter reserves of NO_x and hydrocarbons [6]. It is believed that the background O_3 concentration in the late 19th century was $\approx$20 ppb [6]. In the last three decades, the background O_3 concentration has nearly doubled [6]. It is expected to exceed 40 ppb by 2040, negatively impacting crop yields [6]. If 40 ppb is reached, cyclic variations would increase the likelihood of exceeding the 80 ppb TLV [6].

O_3 is highly reactive and has negative effects on health [7]. It degrades the respiratory system, leading to conditions such as asthma and increased lung infections [7]. Exposure to the gas will worsen pre-existing respiratory conditions [7]. It will also degrade the cardiovascular system, increasing heart rate and diastolic pressure. Long term exposure leads to the same detrimental health effect [7].

2.2 Plasmonic Sensing

2.2.1 Bulk Optical Properties of Metals

To understand plasmonic sensing, it is essential to understand the electronic properties of metals. An approximation, known as the Drude model, can be used to explain the interaction of metals with light [8]. This model assumes that the electrons do not interact with each other [8]. It is assumed the atomic cores are positively charged and do not affect the electrons, unless there is a collision [8]. This is known as the free electron approximation [8]. The Drude model also assumes that electrons are in thermal equilibrium [8].

Light is described by a plane wave (equation 2.1) [8].

$$\varepsilon(z,t) = \varepsilon_0 e^{ikz-\omega t} \tag{2.1}$$

With k being the wave number $k = \frac{2\pi N}{\lambda}$, $N = \sqrt{\epsilon} = \sqrt{\epsilon_r + i\epsilon_i}$, ϵ is the dielectric function [8]. ε_0 is the amplitude, z is the direction of propagation, ω being the frequency and t is time [8].

The next step is to insert the equation for the wave number into equation 2.1 [8]. For optical frequencies, the electrons are highly affected and couple to the field of the light [8]. We can solve an equation of motion to find the displacement of the electrons (equation 2.2) [8].

$$m_e \frac{d^2x(t)}{dt^2} = -e\epsilon_0 e^{-i\omega t} \tag{2.2}$$

Where m_e is the mass of an electron, ϵ_0 is the vacuum permittivity and e the elementary charge [8].

The amplitude of the electron displacement can be solved using an ansatz inserted into equation 2.3 [8]. $x(t) = Ae^{-i\omega t}$ in this case, with A being the complex amplitude [8]. The solution is shown in equation 2.3 [8].

$$A = \frac{e\varepsilon_0}{m_e\omega^2} \tag{2.3}$$

With n being the conduction electron density, the polarization is $P(t) = -nex(t)$ [8]. The dielectric function can be described in terms of the dielectric displacement field $D = \epsilon_0\varepsilon + P$, ε describes the electric field [8]. Which, if rearranged in terms of ϵ and the expression for polarization inserted into equation 2.3, gives a dielectric function as shown in equation 2.4 [8].

$$\epsilon = 1 - \frac{ne^2}{\epsilon_0 m_e \omega^2} = 1 - \frac{\omega_P^2}{w^2} \tag{2.4}$$

w_p is the plasma frequency [8]. When $\omega < \omega_P$, the dielectric function is real and negative [8]. In this case, it observes the same behaviour as a damped wave [8]. In fact, this means the metal reflects the light [8]. In the other case, the dielectric function is real and positive and the metal transmits the light [8].

2.2.2 Localised Surface Plasmon Resonance (LSPR)

The coupling between the electric field of the incident light and the electron plasma in the metal causes the electron to oscillate [9]. These plasma oscillations are propagating quasiparticles, they are called plasmons [3]. Plasmons that propagate on a surface are known as surface plasmons [3]. Localised surface plasmons (LSP) are bound to a nanoparticle [3]. Due to energy and momentum conservation laws, the creation of a surface plasmon can only be achieved with certain configurations [3]. This is not the case for plasmons confined to metallic nanoparticles, as they can be excited by the light directly [3].

Metallic nanoparticles are of interest, as they show significant detectable effects from the increased adsorption/scattering efficiency of the incident light, at certain wavelengths [3]. This creates an extinction peak that is sensitive to changes in the dielectric environment. This peak is created at the resonant frequency, which is described in equation 2.5 [3].

$$\omega_0 = \frac{\omega_0}{\sqrt{1 - 2\epsilon_d}} \tag{2.5}$$

With ϵ_d being the dielectric function of the medium and ω_0, the resonant frequency [3].

The plasmon can be thought of as an oscillating dipole. Creating a very short range, intense, electromagnetic dipole field around the nanoparticle [3]. This field is highly sensitive to changes in the dielectric environment and can be used for sensing [3]. From equation 2.5, a red shift will occur if the dielectric constant of the surrounding is increased [3]. The analyte screens the charges on the surface, causing a shift in the extinction peak [3]. The extinction peak is also affected by the temperature of the nanoparticles [3].

The sensitivity of the plasmon to changes is dependent on the ease of polarizability [3]. The shape of the nanoparticle will determine the geometry of the generated dipole field, which affects the sensitivity as well [3].

The sensitivity of a plasmonic sensor is the peak shift ($\delta\lambda$) per refractive index unit (RIU)(δn), shown in equation 2.6 [3]. A value known as the figure of merit (equation 2.7) additionally takes into account the broadness of the peak (FWHM) [3]. Peak shifts are more visible for narrow peaks [3]. The sensitivity can also be expressed as peak shift per concentration, rather than refractive index units [3].

$$\sigma = \frac{\delta\lambda}{\delta n} \tag{2.6}$$

$$FOM = \frac{\frac{\delta\lambda}{\delta n}}{FWHM} \tag{2.7}$$

The sensitivity of these sensors is improved by using a metal oxide thin film coating [4][3]. In this case, the film interacts directly with the gases of interest [4].

2.3 WO_3 Properties and Sensing

2.3.1 Crystallographic Properties

WO_3 is an n-doped semiconductor [10]. It occurs in a monoclinic phase between 17°C and 350°C, below 17°C, the triclinic phase is stable [11]. Each W atom is coordinated in a sixfold fashion to each of the oxygen atoms [10]. Oxygen vacancies in the lattice affect the morphology and interact with adsorbing gases [4], adsorbed oxygen species can also be a point of interaction [4].

Changes in resistivity are mediated by oxygen vacancies and surface adsorbed oxygen species [12][4]. A change in resistivity will directly affect the dielectric function of the film [10]. Which also changes the dielectric function around the nanoparticle, causing a shift in the extinction peak [4].

At room temperature, or in an oxidising environment, oxygen adsorbates are present at grain boundaries and on the surface of the film [13]. The adsorbed oxygens deplete the conduction band of n-doping electrons, forming O^- O^{2-} $O_2{}^-$ [4]. This creates a space charge region of one Debye length [14]. An oxidising gas can interact with the adsorbed species or an oxygen vacancy [4]. The adsorbing gas oxidises the surface [4]. This further increases the size of the space charge region, thus reducing the amount of conduction electrons available and increasing the resistivity [4]. The reverse occurs in a reducing atmosphere [15].

While this is true for any oxidising gases [4]. It is interesting to look at NO_2 and O_3 in more detail. This is covered in sections 2.3.3 and 2.3.4.

2.3.2 Vacancies and Oxygen Partial Pressure

The oxygen partial pressure and temperature of the system influence the amount of oxygen vacancies on the WO_3 surface [12]. This is described by the reversible equation 2.8 [12].

$$\mathrm{WO_3} \underset{\mathrm{k_2}}{\overset{\mathrm{k_1}}{\leftrightarrow}} \mathrm{V}^{\circ} + \mathrm{WO_{3-1}} + \frac{1}{2}\,\mathrm{O_2} \tag{2.8}$$

In the vacancy (V°), there are two free electrons present [12]. Through ionisation, they can be excited into the conduction band [12]. The complete equilibrium can be described by equation 2.9 [12].

$$\mathrm{WO_3} \xleftrightarrow[\mathrm{k_2}]{\mathrm{k_1}} \mathrm{V}^{\circ 2+} + \mathrm{WO_{3-1}} + \frac{1}{2}\,\mathrm{O_2} + 2\,\mathrm{e} \tag{2.9}$$

From observing equation 2.9, the oxygen partial pressure must influence the density of oxygen vacancies, higher oxygen partial pressure shifts the equilibrium to the left. Temperature is also a factor, since thermal energy is required to excite electrons into the conduction band [12], the activation energy required can be derived from the slope of an Arrhenius plot of resistivity and temperature (figure 2.1) [12].

A decrease in oxygen partial pressure also decreases the activation energy for the ionisation of the donor species [12]. This decrease in activation energy can be explained by the presence of a defect band [12]. Increased vacancies lead to more donor species present at the vacancy sites [12]. The orbitals of the donors start to overlap, eventually forming a new band (the defect band) [12]. This decreases the band gap [12]. A decreasing band gap means less activation energy is required to excite an electron into the conduction band [12].

However, at a O_2 partial pressure of 1 bar, above 200°C, oxygen adsorption leads to a decrease in the amount of vacancies, this leads to a resistivity increase [12]. Other adsorbates are also of concern, for example H_2O, which remains adsorbed, up to ≈150°C [12]. The O_2 partial pressure during annealing is also important, if it is too low, interstitial tungsten can be created, increasing activation energy [16].

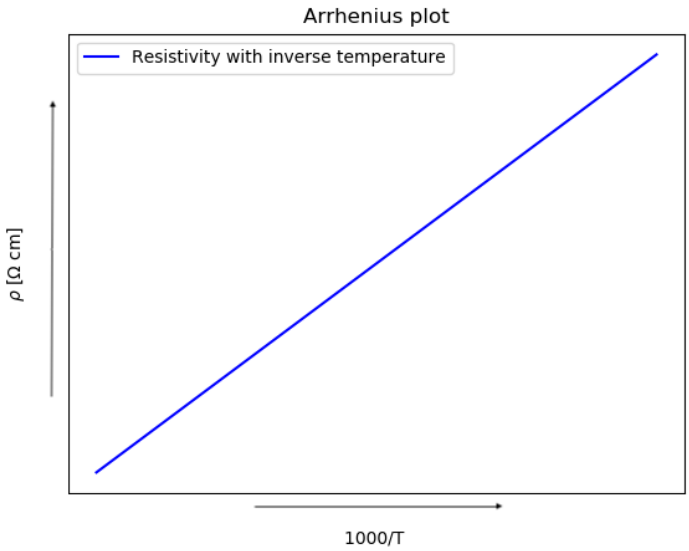

Figure 2.1: General shape of an Arrhenius plot of resistivity according to inverse temperature, the gradient of the curve is the activation energy required.

2.3.3 NO_2 Sensing on WO_3

There are two adsorption pathways for NO_2 [10]. The first possibility is when the central nitrogen interacts with an oxygen vacancy [10]. Density functional theory (DFT) calculations show that in this case the adsorption energy is very small [10]. The molecule only remains weakly chemisorbed, with little charge transfer from the surface to the NO_2 [10]. As the electronic configuration of the surface remains nearly unchanged, the sensor would not be able to detect NO_2 adsorbing in this configuration [10].

When one of the oxygen atoms in the NO_2 molecule (O_g) interacts with an oxygen vacancy, the molecule can be considered nearly dissociated [10]. The bond length between O_g and the nitrogen increases, while the other bond length (NO^*) decreases significantly [10]. The interaction of NO^* with the surface creates a charge neutral situation [10]. No change is detectable until the NO^* reforms NO_2 [10].

The NO^* remaining above the surface reforms NO_2 from interacting with an O_2. Once NO_2 is reformed, O_g is left in the vacancy [10].

$$WO_{3-1} + V^{\circ} + NO_2 \longrightarrow WO_3 + NO^* \tag{2.10}$$

$$WO_3 + NO^* + \frac{1}{2}O_2 \longrightarrow WO_3 + NO_2 \tag{2.11}$$

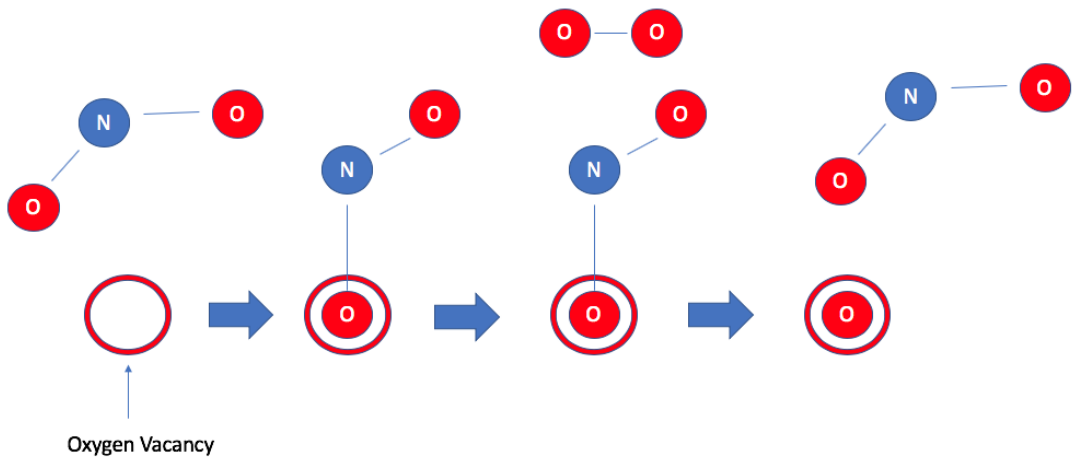

Figure 2.2: Graphical representation of NO_2 adsorption into an oxygen vacancy present on the WO_3 surface.

Equations 2.10, 2.11 describe the adsorption process [10]. A schematic of the process in shown in figure 2.2

Once the NO* reforms NO_2, the vacancy is occupied [10]. The WO_3 surface loses a conduction electron [10]. The space charge region increases [4]. The density of state shifts towards the valence band, and the resistivity increases [10], changing the dielectric medium around the nanoparticle. The adsorption with a surface oxygen adsorbate species is the same as described above [10].

2.3.4 O_3 Sensing on WO_3

The geometries for the interaction of O_3 with a WO_3 surface are similar to NO_2, and can be determined through DFT calculations [17].

If the position of the O_3 molecule is initially horizontal, the central oxygen atom will interact with the oxygen vacancy [17]. As this is such a weak interaction, it only negligibly affects the resistivity [17].

For a vertical molecule, one of the side oxygens interact with the WO_3 surface, in the same way as when the side oxygens of NO_2 interact with the WO_3 surface [17]. The adsorption pathway of O_3 is summarised in equation 2.12 [17]. A schematic of this process is summarised in figure 2.3

$$WO_{3-1} + V^{\circ} + O_3 \longrightarrow WO_3 + O_2 \tag{2.12}$$

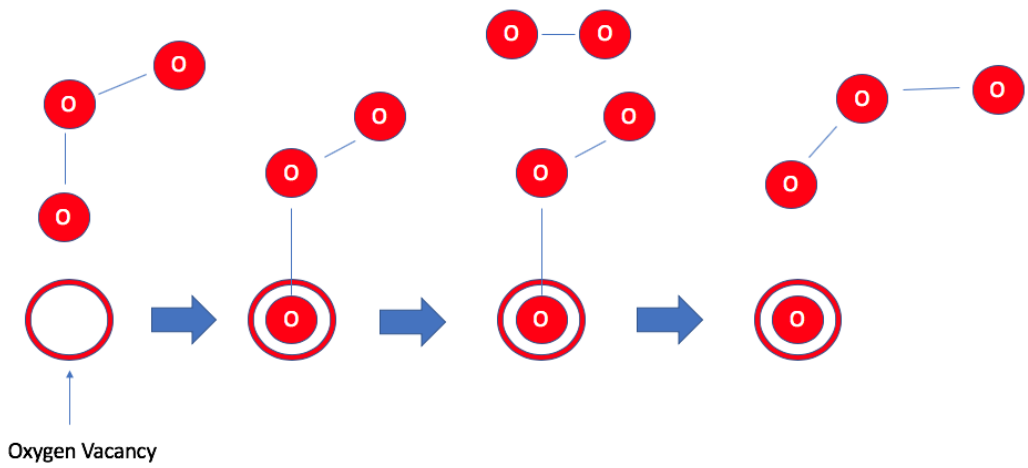

Figure 2.3: Graphical representation of O_3 adsorption into an oxygen vacancy present on the WO_3 surface.

The highest sensitivity to O_3 for WO_3 resistive sensors is achieved between 473K and 573K [16], with a maximum at 537K [15]. At a constant temperature, the coverage of O_3 on the surface increases with concentration [15]. This is to be expected, since the dissociation of O_3 is more exothermic than for NO_2 [10][17]. The maximum temperature of the X1 reactor used in this study is 350°C. At this temperature, the surface coverage of O_3 would be approximately 0.1% when exposed to 100 ppb

of O_3 [15]. If only synthetic air is present, the surface coverage from the possible adsorbates is $10^{-4}\%$ [15]. As temperature increases, O_3 adsorption is preferred over synthetic air species [15].

2.4 Production of the Nanoplasmonic Sensor

The sensor was produced using hole mask colloidal lithography (HCL). The process is describe below:

- A poly(methyl methacrylate)(PMMA) layer is first spin coated onto a glass or silicon substrate [18].
- In order to increase hydrophilicity, the PMMA is etched for a short time using an O_2 plasma [18]. A polyelectrolyte solution is subsequently pipetted onto the surface to create an adhesive layer [18].
- A solution of charged polystyrene colloids is then introduced to the surface. The colloids are repelled by each other, but are attracted to the surface, forming an organised pattern [18].
- After a drying period, a thin film is deposited onto the structure [18]. This thin film needs to be resistant to O_2 plasma [18].
- The beads are removed using tape stripping, in this process, adhesive tape is stuck to the surface and removed, thereby removing the beads [18].
- The removal of the beads exposes the PMMA in the areas where the beads were [18]. O_2 plasma is used once again to create wells through the PMMA layer [18]. Other plasma's such as CF_4 can also be used, if the wells need to be extended into the substrate [18].
- Material can now be deposited into the wells [18]. For example, physical vapour deposition (PVD). Different angles can be used to achieve certain nanoparticle shapes [18].
- A final step involves a lift off process performed in acetone to remove the wells [18]. The finished product can then be diced, creating individual sensors.

The sensors used in this study sensors are composed of nanodiscs. They are far enough apart to avoid any near field enhancements.

The metal oxide film can now be deposited on the nanoparticles using magnetron sputtering. In the sputtering process, high energy electrons originating from an O_2 plasma bombard a target, causing the ejection of atoms which then deposit themselves as a thin film on the target [19].

Secondary electrons are also generated that contribute to maintaining the plasma [19]. A magnetic field concentrates a plasma on the substrate, improving the adhe-

sion of the material onto the surface [19]. As a final step the sensors are annealed.

A schematic of the architecture of the sensor is shown in figure 2.4.

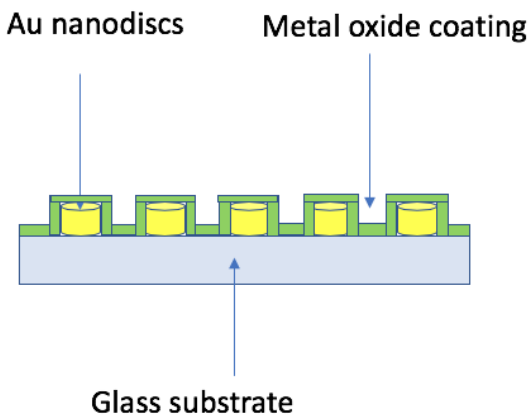

Figure 2.4: Schematic of the sensor Architecture.

2.5 Sensor Behaviour

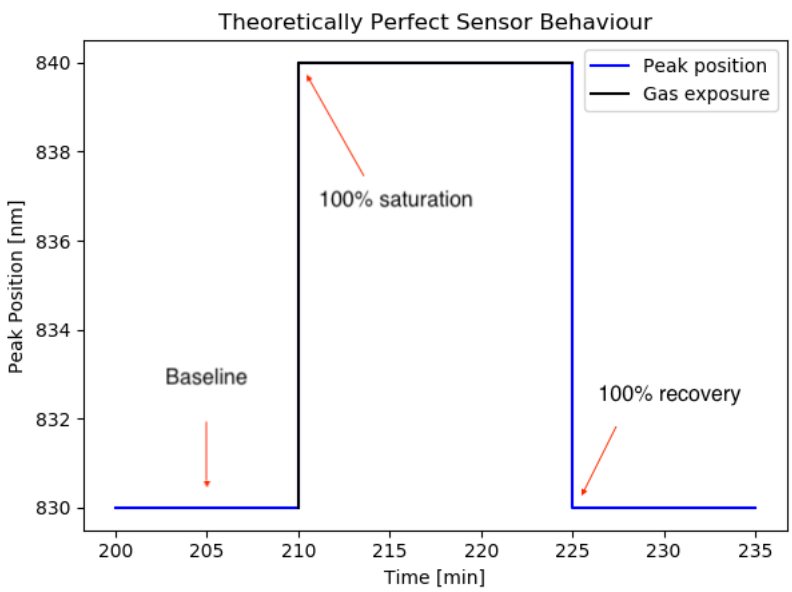

Figure 2.5: Behaviour of a theoretically perfect sensor.

The behaviour of a theoretically perfect sensor is shown in figure 2.5. It resembles a square wave. The initial peak position is called the baseline (830 nm in figure 2.5). The plateau reached after gas exposure (at 840 nm in figure 2.5) indicates that the sensor has reached saturation i.e the maximum change in peak position. The time taken to reach 90% saturation (the t_90) is called the response time. The time taken

to return to the baseline is the recovery time. In reality, the sensor will not always return to the baseline, this is called drift.

The black line in figure 2.5 represents an exposure. An exposure is when the gas of interest is present in the system. The same black line is used in the results to separate out the exposures from the rest of the data. The combined exposure and recovery is referred to as a cycle.

3

Methods

3.1 Description of the Experimental Setup

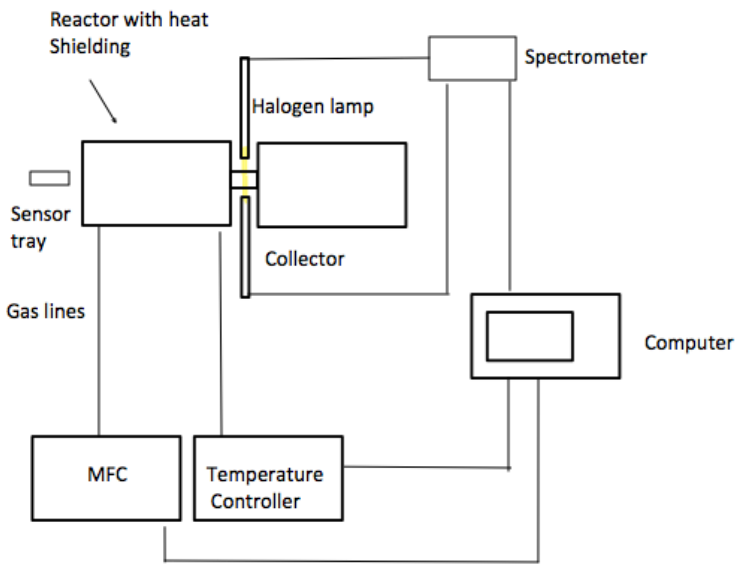

Figure 3.1: Schematic of the Insplorion X1 reactor.

The experiments were performed using the Insplorion X1 reactor. A schematic of the setup is shown in figure 3.1. A sensor is placed within the slot and inserted into the reactor. A light source illuminates the sensor through an opening in the chamber, the data is collected by a spectrometer. A proprietary algorithm extracts the peak position from the spectrometer data. The flow of gas is controlled by mass flow controllers (MFC), and the desired temperature of the setup is adjusted using a temperature controller.

Before the experiment begins a piece of fused silica is placed in the reactor, a baseline is recorded using the spectrometer. This is done to negate the effects of the glass substrate on which the sensor is built.

The sensor is then inserted and a stabilisation performed. In this step, conducted at 300°C, a mixture of N_2 and O_2 at atmospheric composition is injected into the system, this mixture is known as synthetic air. This procedure is used to clean the sensor.

During a cycle, the gas of interest is introduced for a predetermined amount of time, with the synthetic air used as a carrier gas. The flow rate of the synthetic air is adjusted to match the flow rate of the gas of interest, to keep the flow rate constant. During the second half of the cycle (recovery phase), 100% synthetic air flows through the system.

The O_3 was produced using a generator that takes in ambient air through a pump connected to a flow meter. The flow is adjusted using a knob and a levitating ball bearing scale. The O_3 concentration is adjusted using a potentiometer, numbered according to the concentration desired. The gas flows through a tube and is exposed to a UV lamp, the power of which is adjusted by the potentiometer. The output is then passed through a tube to the X1 reactor. A schematic is shown in figure 3.2.

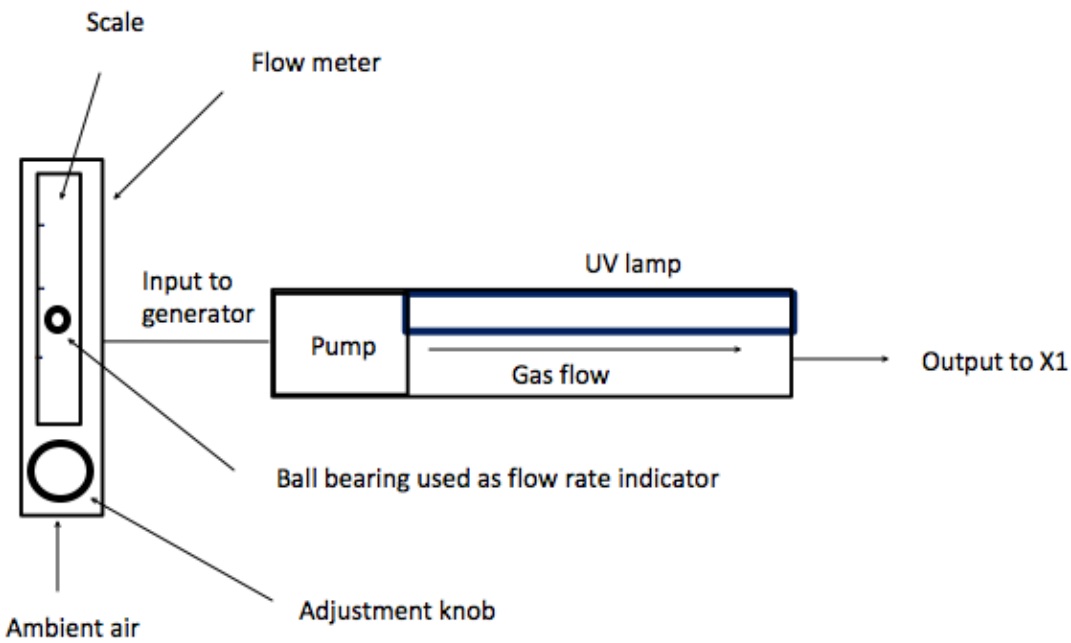

Figure 3.2: Schematic of the Ozone generator.

3.1.1 List of Experiments

1. A temperature sweep was conducted to determine how the sensor reacts to different temperatures. This was achieved by exposing the sensor to 2 exposures of 100 ppb NO_2, for 2 hours each, in temperature steps of 20°C from 120°C to 320°C.

2. To investigate the response of the sensor to different concentrations of NO_2; an NO_2 concentration sweep was performed. In this experiment, the sensor was exposed to concentrations of 10,20,50,100 and 500 ppb of NO_2 in sets of 3 exposures of 2 hours each. The reactor was set to 250 °C throughout the measurement.

3. To achieve an understanding of the response of the sensor to different temperatures in an O_3 environment; an O_3 temperature sweep was performed. The sensor was exposed in single exposures of 15 minutes, at a constant concentration of 50 ppb O_3, in temperature steps of 20°C, from 160°C to 320°C.

4. To explore the behaviour of the sensor to different concentrations of O_3; an O_3 concentration sweep was performed. With concentrations ranging from 30 to 100 ppb in steps of 10 ppb, with one 15 minutes exposure per concentration step. The reactor temperature was 250°C.

5. An experiment was performed to study whether NO_2 could be detected in a 20 ppb O_3 background. The sensor was exposed to three 2-hour exposures of 1 ppm NO_2. Followed by six 2-hour exposures with 20 ppb of O_3 background. The measurements were performed at a reactor temperature of 250°C.

6. To investigate NO_2 sensing in a 40 ppb O_3 background; the sensor was exposed first to four, 2-hour exposures of 1 ppm NO_2. After the introduction of a 40 ppb O_3 background, four additional, 2 hour NO_2 exposures were conducted. With the reactor temperature being 250°C throughout the whole experiment.

7. The ability of the sensor to detect NO_2 with an 80 ppb O_3 background was investigated. The sensor was first exposed to 2 exposures of 1 ppm NO_2, each 2 hours in duration. After which 80 ppb O_3 was introduced as a constant background, the sensor was then exposed to 1 ppm NO_2, for 3 cycles. The O_3 background was removed, the last 4 exposures were 2 hours in duration, at 1 ppm NO_2 concentration. This experiment was also performed at a reactor temperature of 250 °C.

8. Additionally, a further temperature sweep was performed from 160°C to 300°C in steps of 20°C with both NO_2 at 100 ppb and O_3 at 40 ppb. This appears in Appendix C.

It is worth noting that discrepancies do appear between the temperatures stated above and the ones presented in the data. This is due to the fact that the sample temperature was selected for processing rather than the reactor temperature. This was done in the interest of precision. The errors in any gathered data are reported as one standard deviation.

4

Results

4.1 Temperature & Concentration Sweep NO_2

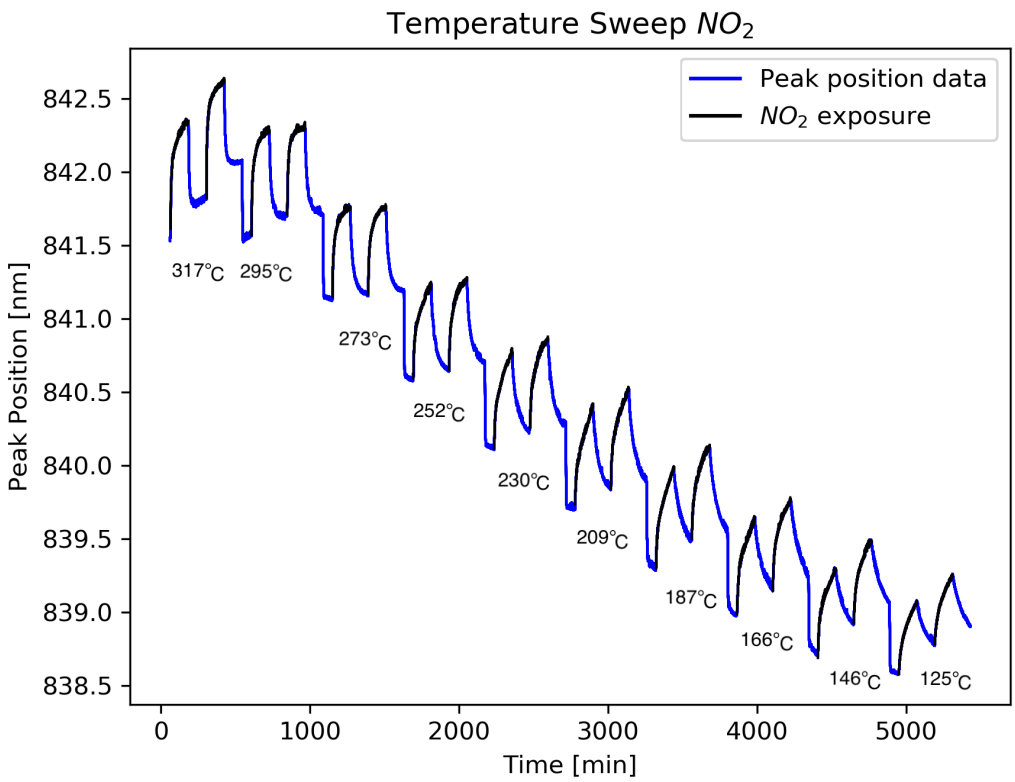

Figure 4.1: NO_2 Temperature sweep in 20°C steps with each gas exposure denoted as black lines, constant concentration of 100 ppb for each cycle.

The result of the NO_2 temperature sweep appears in figure 4.1. A full comparison between O_3 and NO_2 is presented in section 4.3 for improved clarity.

At temperatures above 250°C, both exposures conducted at the same temperature, reach a plateau, indicating they are closer to saturation. An increased peak shift as temperature increases is also visible when comparing the exposures conducted at

125°C and 317°C. In general, the gradient of the exposures steepens with temperature. Therefore, higher temperature improves kinetics.

Significant drift is observed as temperature increases. This effect is caused by the fact that the baseline is different for each temperature step.

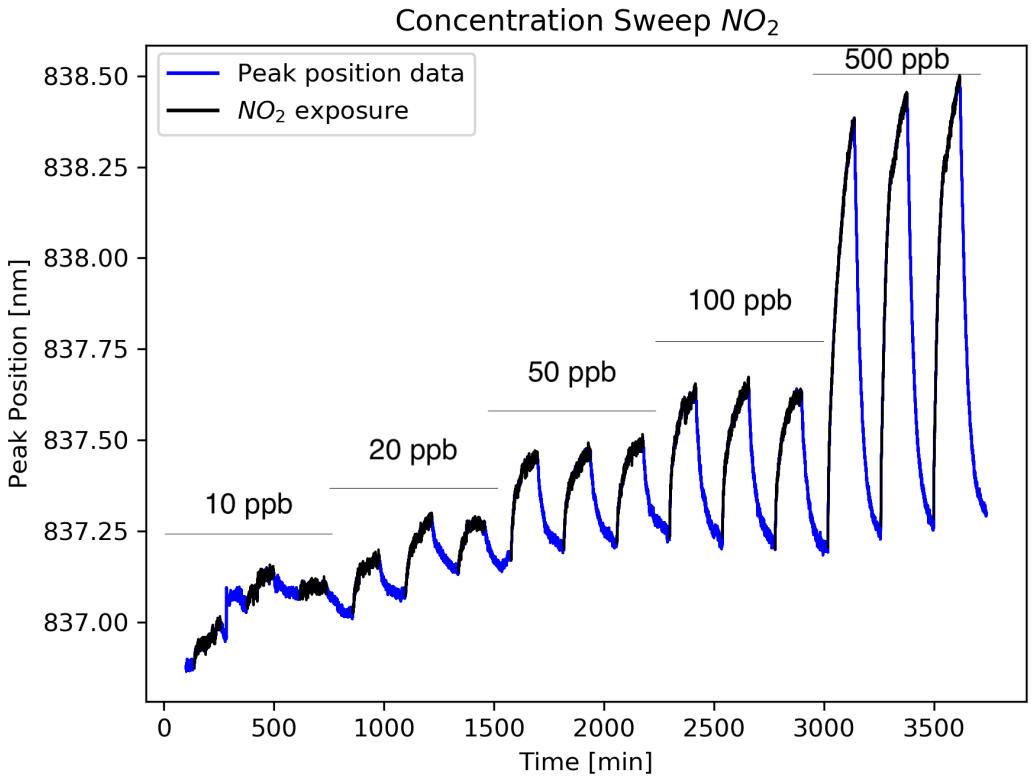

Figure 4.2: NO_2 Concentration sweep, 10-100 ppb, 10 ppb steps, 3 exposures of 2 hours each per concentration step, 250°C constant reactor temperature.

For the NO_2 concentration sweep in figure 4.2, the behaviour of the sensor for the first 3 exposures, conducted with 10 ppb NO_2, is particularly poor. The peak position change is negligible and drowned out by noise. It is difficult to extract any useful information. The low concentration of NO_2 and 250°C reactor temperature, contribute to poor surface coverage of the target gas and high desorption probability, respectively. Leading to a highly variable and noisy signal. However, for each subsequent exposure in sets of 3 at 20,50,100 and 500 ppb NO_2 respectively, a clear improvement is observed. The exposures are well defined, with the 500 ppb measurements showing the most change in peak position of ≈1.5 nm.

4.2 Temperature & Concentration Sweep O_3

The general observable trend in figure 4.3, is that at lower temperatures, the peak shifts are lower in magnitude, but reach a plateau faster. With the exposure at 125 °C having plateaued out the fastest. The same drift from temperature changes seen in figure 4.1 is apparent here. Small plateaus before each exposure appear, these correspond to the new baseline at each temperature step.

From this it can be determined that, while higher temperature improves kinetics, it does introduce instability. This can be seen in the variations in the plateaus of the higher temperature exposures, these variations increase with temperature.

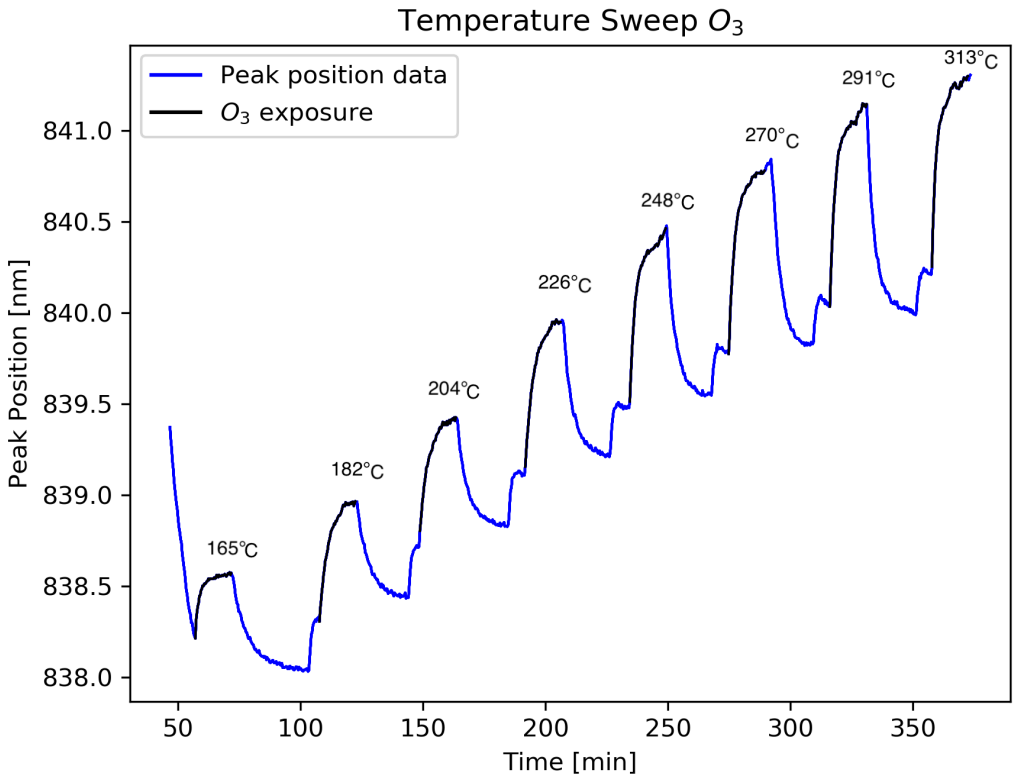

Figure 4.3: Temperature sweep for O_3, in steps of 20°C, constant 50 ppb O_3 concentration for each cycle, 15 minutes exposure per cycle. 250°C reactor temperature.

The O_3 concentration sweep in figure 4.4, shows distinctly different behaviour compared to the NO_2 concentration sweep (figure 4.2). Plateaus are reached within 15 minutes from observing the plot, indicating the exposures are close to saturation, and therefore improved response time over NO_2. Additionally, the peak shifts observed are much greater in magnitude and more clearly defined, compared to similar NO_2 concentrations.

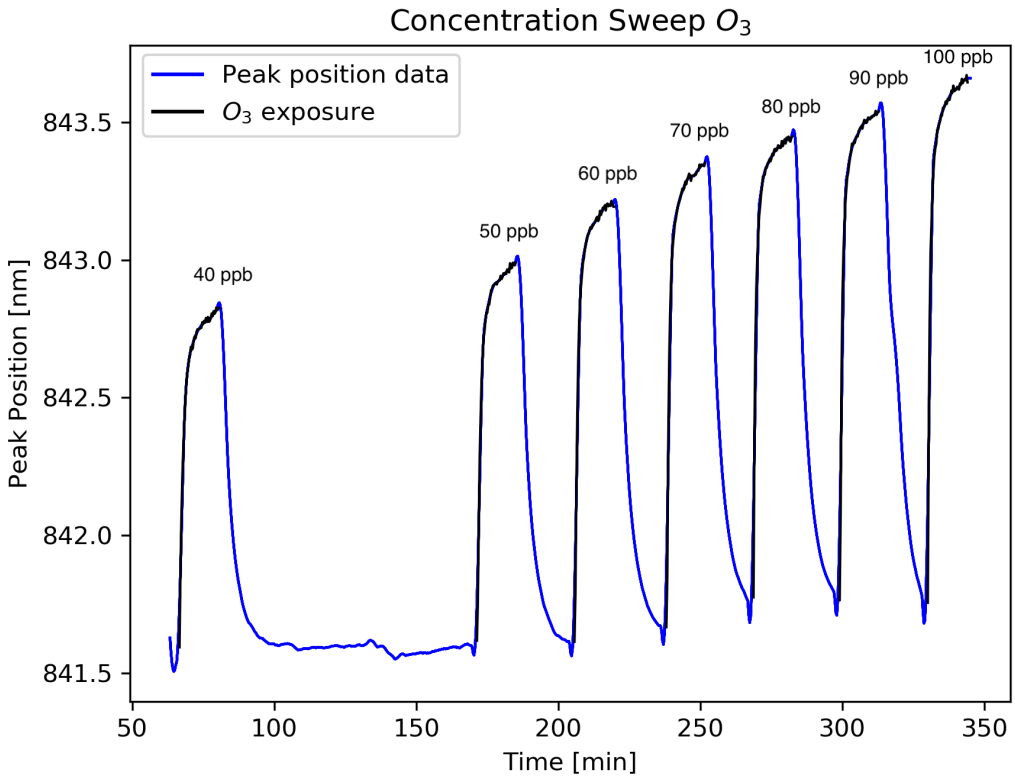

Figure 4.4: O_3 Concentration sweep, 40-100 ppb, 10 ppb steps, 1 exposures of 15 minutes per concentration step, 250°C constant reactor temperature.

A clear trend is visible in an almost perfectly linear peak shift increase, between the different concentrations, outweighing the slight drift observed. This slight drift indicates that the sensor has not completely recovered before the new exposure begins. This trend is apparent throughout this study, indicating that longer exposure and recovery times were needed. Therefore further study would be needed to confirm the findings of this work.

4.3 Comparison Between O_3 and NO_2

The comparison of the peak shift for the concentration range of 10 ppb to 100 ppb for NO_2 and 40-100 pbb for O_3 is shown in figure 4.5.

The data shown in figure 4.5, is the difference in peak position between the starting and ending points of the measurements. An apparent linear trend can be seen for NO_2, despite the larger errors at the concentrations of 10 ppb and 20 ppb. For the concentrations of 50 ppb and 100 ppb however, the data is consistent and barely shows any error. It is worth noting the 500 ppb point has been removed in the interest of scaling. The peak shift varies in a small range from less that 0.1 nm at 20 ppb to 0.4 nm at 100 ppb.

In comparison, the O_3 peak shift data shows a similar linear trend. However, the peak shifts are much greater in magnitude, compared to the same concentration of NO_2, starting at 1 nm for 30 ppb of Ozone, up to nearly 2 nm for 100 ppb.

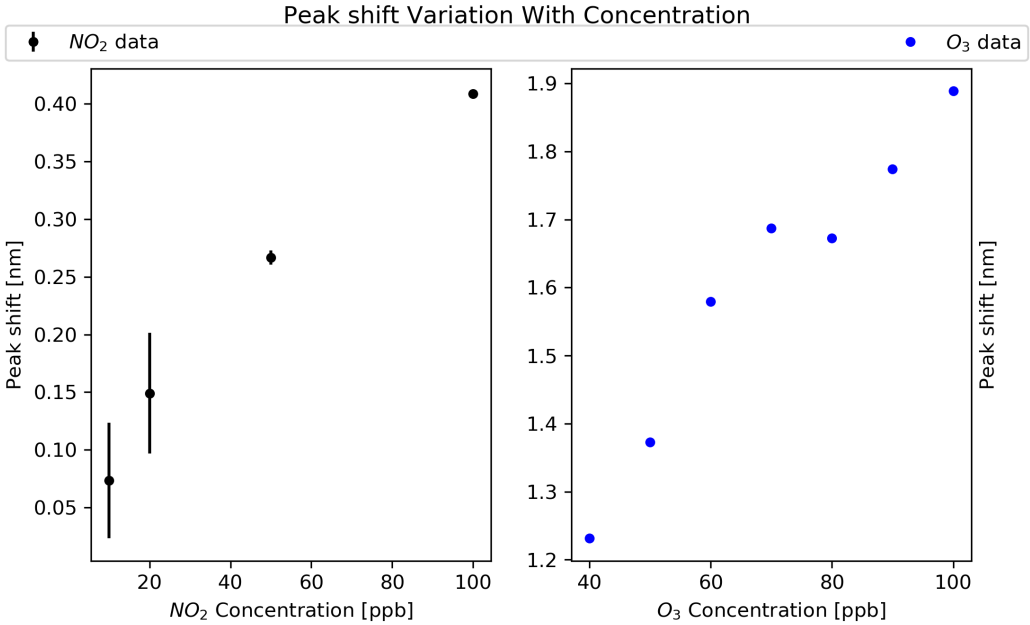

Figure 4.5: Variation of peak shift with concentration, for the range 10-100 ppb for NO_2 (left), and 40-100 ppb for O_3 (right).

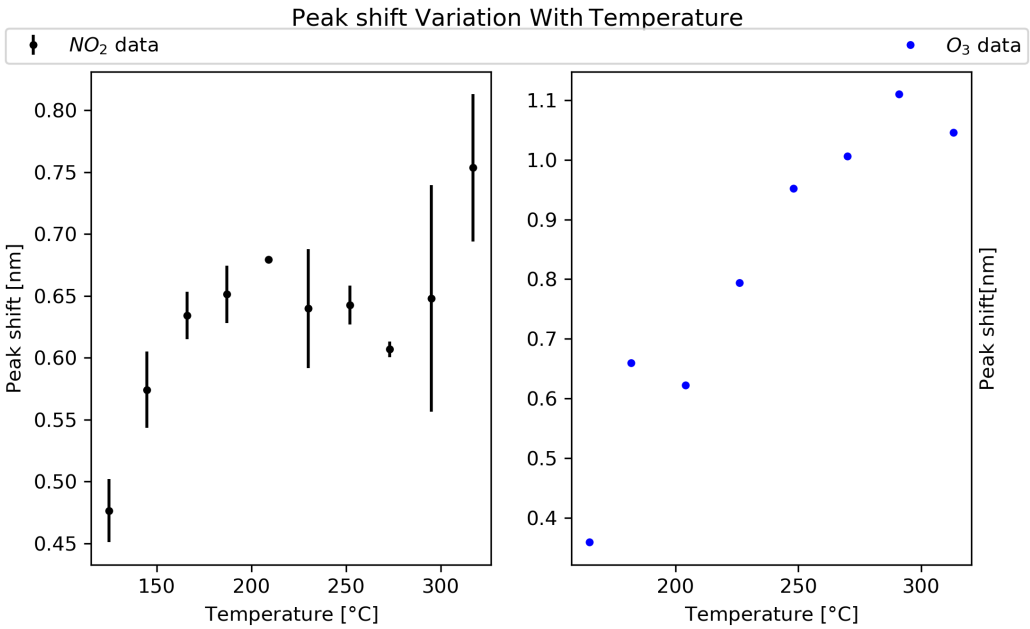

Figure 4.6: Variation of peak shift with temperature, NO_2 at 100 ppb on the left, O_3 at 50 ppb on the right.

In figure 4.6, the data for NO_2 shows a maximum at 209°C with an additional

maximum reached at 317°C. Noise is a contributing factor for the points at 295°C and 317 °C, as well as the fact that this is outside the regular operating range of the sensor.

With regards to the O_3 data, a general increase is observed with the maximum likely appearing at 291 °C. This data does confirm previous research showing that the best temperature for O_3 sensing is 300°C [15].

According to this data, the ideal operating temperature for NO_2 would be setting the reactor temperature to 200°C. For O_3, 300°C is the most suitable temperature.

4.4 NO_2 With 20 ppb O_3 Background

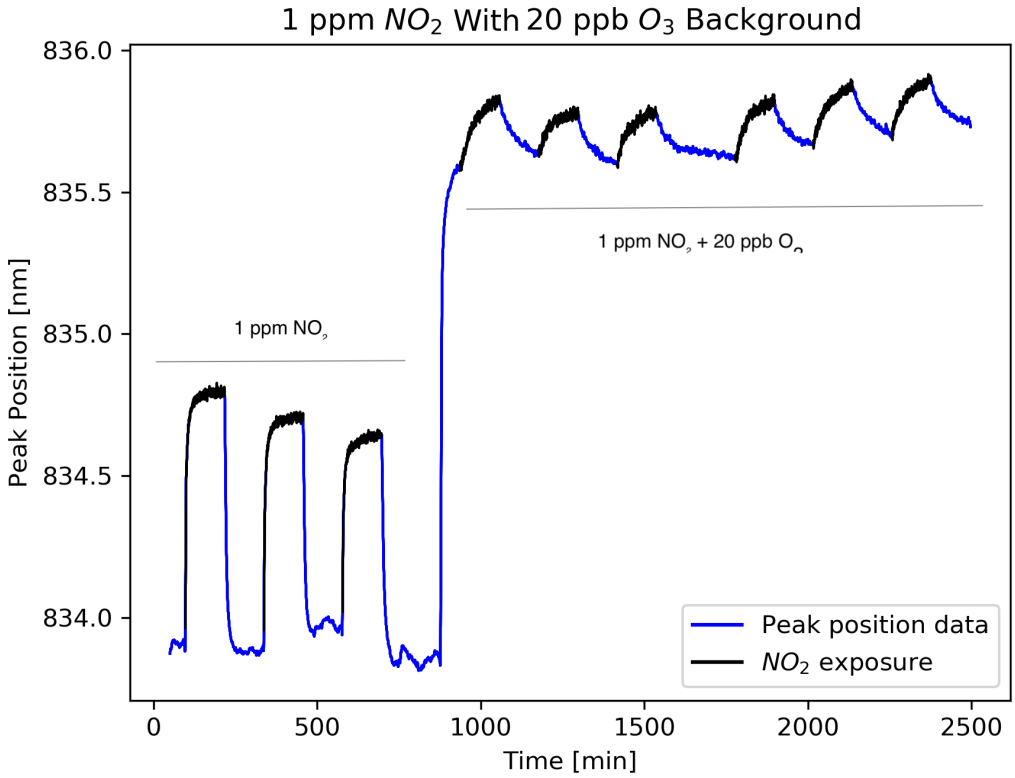

Figure 4.7: 1 ppm NO_2 with 20 ppb O_3 background, first 3 measurements exposed to only 1 ppm NO_2, last six exposures to 1 ppm NO_2 with a constant 20 ppb O_3 background, reactor temperature of 250°C.

The data is presented in figure 4.7. 4 exposures with O_3 were chosen in this case, to investigate the consistency of the NO_2 detection in an O_3 background over a longer period of time. The 3 first NO_2 exposures qualitatively have reached sustained plateaus, indicating near saturation. Once the O_3 is introduced at a flow rate 0.5 L/min, a significant baseline increase is observed. This flow rate differs from the 1.5

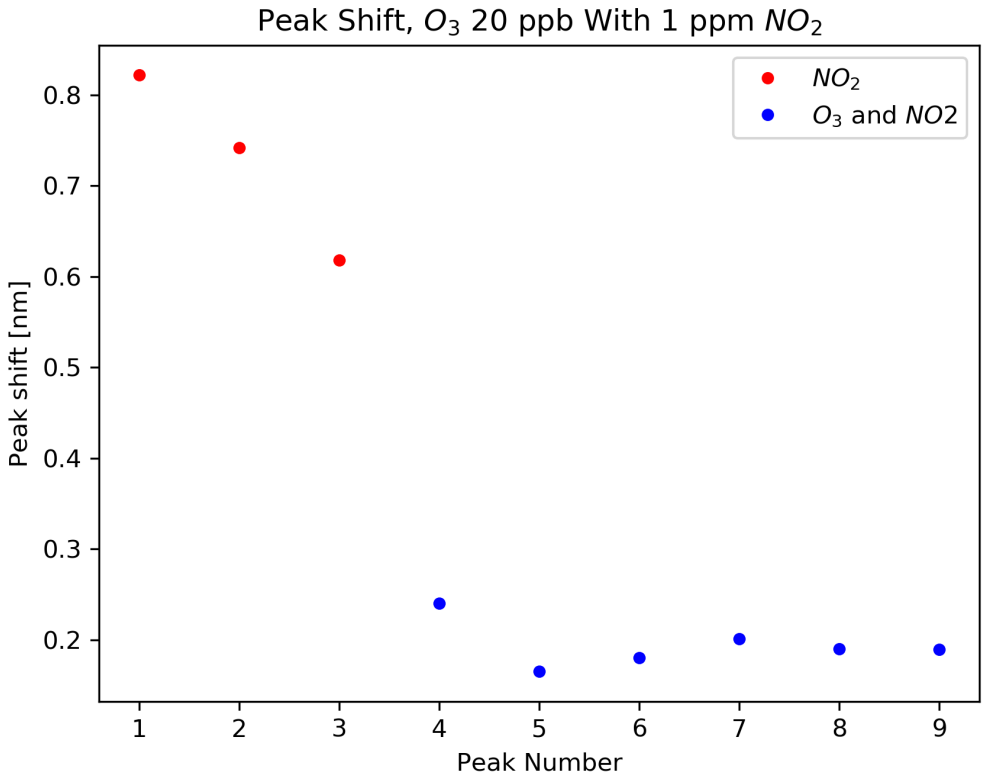

Figure 4.8: Peak shift variation, 1 ppm NO_2 exposures, and 1 ppm NO_2 exposure with a constant 20 ppb O_3 background.

L/min used in the next two experiments. This was done to dilute O_3 down to 20 ppb, the limiting factor was the flow rate of the MFCs. After the introduction of the O_3 background, the exposures with NO_2 are distinctly clear and show little drift. In figure 4.8, the peak shifts for the NO_2 exposures during the 20 ppb O_3 background are consistent at ≈0.2 nm, compared to 0.6-0.8 nm for the exposures conducted without O_3. This sharp decrease when O_3 is present is understandable as a large number of sites are going to be occupied by O_3, even at such low concentrations, due to the significantly higher reactivity of O_3. NO_2 does however occupy some sites, since the NO_2 exposures are visible.

4.5 NO_2 with 40 ppb O_3 Background

In figure 4.9, drift is apparent in the NO_2 exposure after the O_3 is introduced. The NO_2 exposures are less uniform in a 40 ppb O_3 background than in a 20 ppb O_3 background. While the exposures are still distinct, they show erratic behaviour.

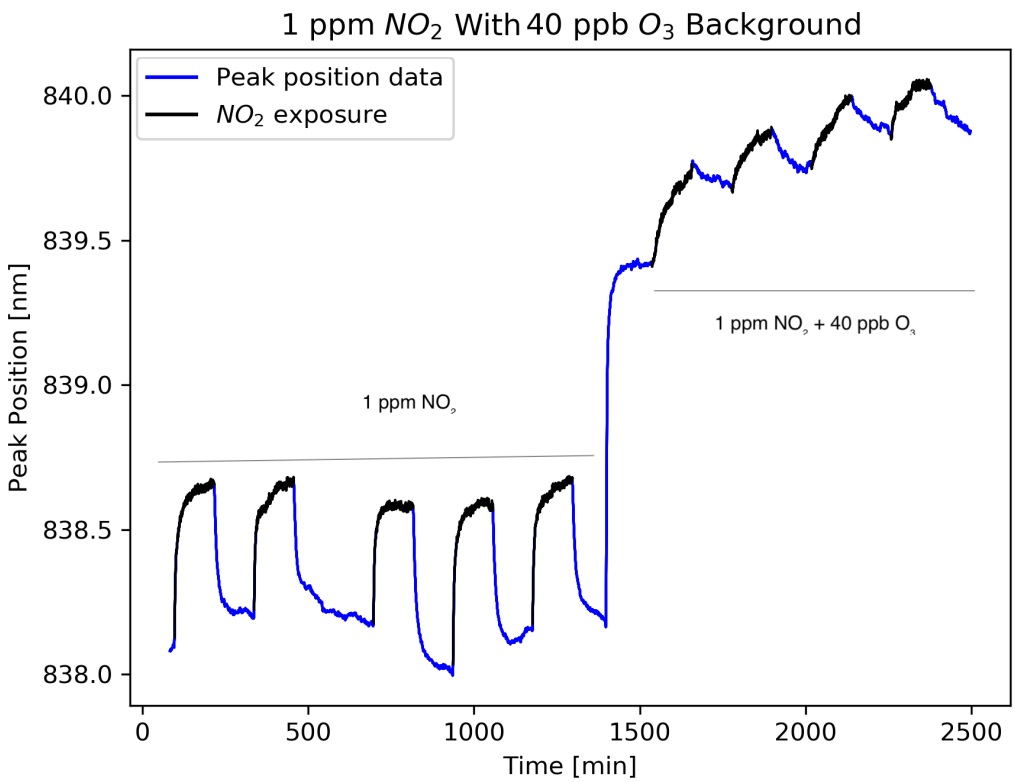

Figure 4.9: 1 ppm NO_2 with 40 ppb O_3 background, first 5 exposures conducted under 1 ppm NO_2 concentration, last 4 exposures to 1 ppm NO_2 with a constant 40 ppb O_3 background, reactor temperature of 250°C.

The 5 exposures at the beginning of the experiment are used to investigate how the measurements conducted in an O_3 background are affected by a greater number of NO_2 cycles before the introduction of the background. The drift is most likely due to the higher O_3 background. A significant variation in the baseline is visible for the first 5 NO_2 exposures, which is apparent in figure 4.10, this could be explained by variations in the system.

The comparison of the NO_2 peak shifts, before and after the O_3 background was introduced is shown in figure 4.10. The variation in baseline and instability clearly appear here in the exposures conducted with pure NO_2. A general decrease is observed for the NO_2 exposure conducted with the 40 ppb O_3 background. The peak shifts in this case are erratic and vary between 0.2 nm and 0.4 nm. This could be explained by the fact that the sensor has not completely recovered after exposure,

reducing the amount of sites for the next exposure, leading to a decrease in peak shift.

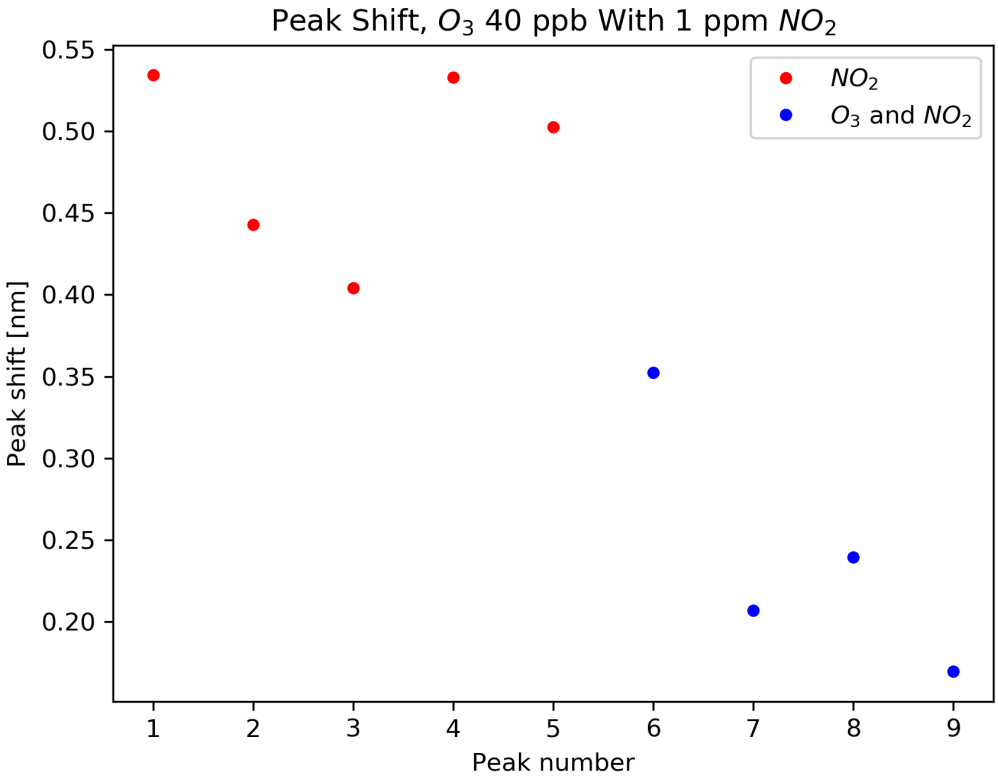

Figure 4.10: Peak shift variation, 1 ppm NO_2 exposures, and 1 ppm NO_2 exposure with a constant 40 ppb O_3 background.

4.6 NO_2 With 80 ppb O_3 Background

In figure 4.11, the exposures conducted with 1 ppm NO_2 have plateaued out, indicating they are close to saturation. This suggests that the sensor has recovered from the O_3 background. However, once the O_3 is removed, the baseline is higher for the final NO_2 measurements. Perhaps some sites are still occupied by O_3, or some O_3 adsorbates remain in the subsurface, increasing the baseline. Another possibility is the sensor was not allocated enough time to completely recover from the O_3 background.

The NO_2 exposures performed with the 80 ppb O_3 background present, exhibit different behaviours to those at 20 ppb and 40 ppb O_3 background. The drift is more pronounced than in the corresponding 40 ppb O_3 background exposures. Furthermore, the exposures are much shallower and barely distinguishable from the drift. The lack of recovery time could be used to explain this. An alternative explanation is that the O_3 poisons the sensor, increasing the recovery time, as it adsorbs to sites previously occupied by NO_2.

It is clear that due to the sensor's high sensitivity to O_3, a solution would need to be developed to shield the sensor, if NO_2 is the target gas.

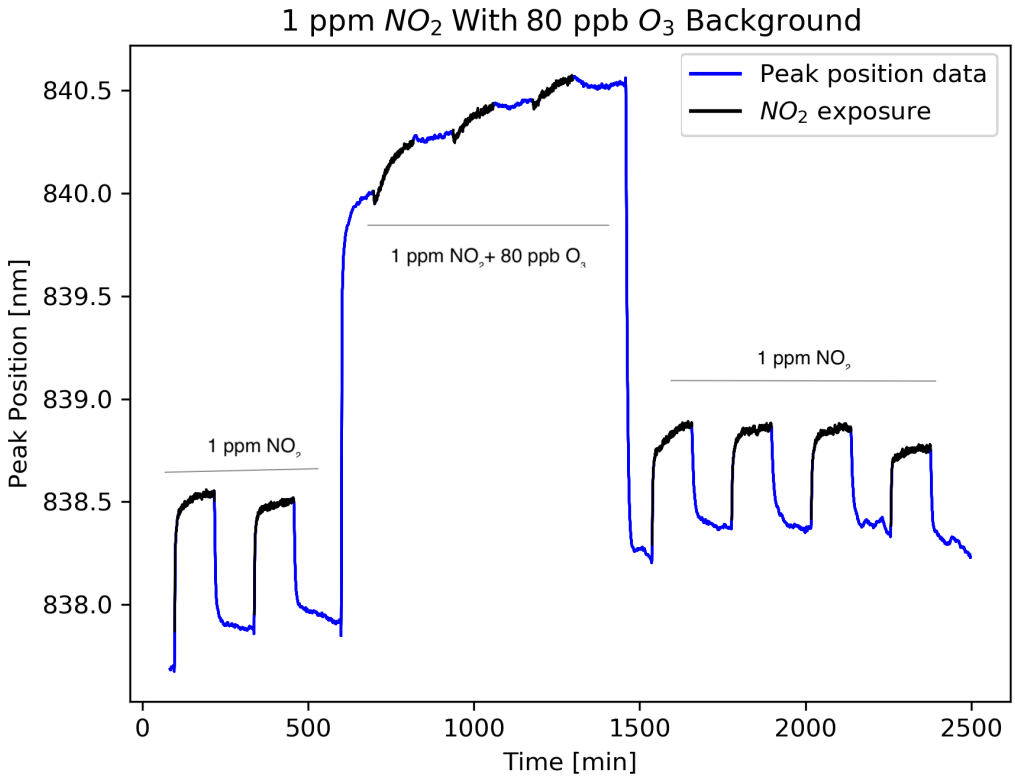

Figure 4.11: 1 ppm NO_2 with 80 ppb O_3 background, first two and last four cycles exposed to only 1 ppm NO_2, middle three exposures to 1 ppm NO_2 with a constant 80 ppb O_3 background, reactor temperature of 250°C.

In the peak shift comparison plot (figure 4.12), the peak shift observed for measurements with only 1 ppm NO_2 show a distinct decrease, both before and after the O_3 background is removed. This indicates that not enough time was allocated to allow the sensor to recover completely from the NO_2 exposures. The same trend is observed for the NO_2 exposures conducted with the 80 ppb O_3 background. This possibly confirms what was mentioned earlier about the lack of recovery time, and O_3 poisoning of the surface.

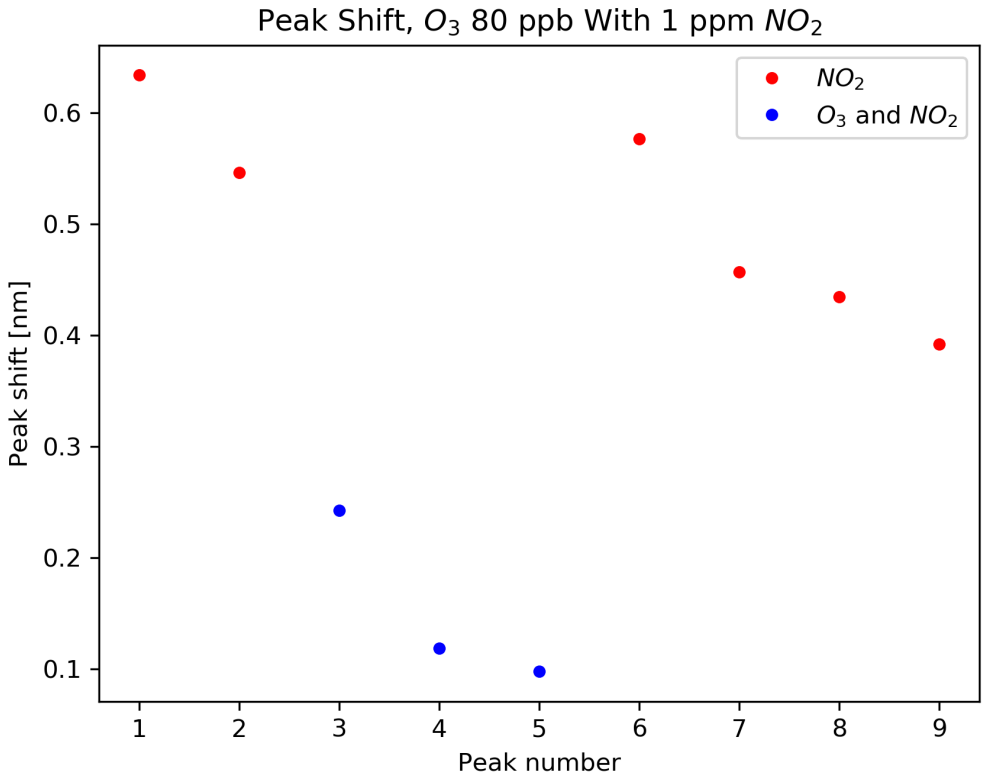

Figure 4.12: Peak shift variation, 1 ppm NO_2 exposures, and 1 ppm NO_2 exposure with a constant 80 ppb O_3 background.

4.7 Comparison of Peak shifts for 1 ppm NO_2 with 20,40 and 80 ppb O_3 backgrounds

The averaged peak shift for 1 ppm NO_2 exposures with 20,40 and 80 ppb O_3 background is shown in figure 4.13. The error increases for each O_3 background step, with lowest error apparent for the 20 ppb O_3 background. While the averages only vary between 0.15 nm for an 80 ppb O_3 background and 0.25 nm for a 40 ppb O_3 background. It is clear that O_3 poisons the sensor and introduces instability.

From this data, and the data in figure 4.8, NO_2 exposures at 1 ppm can only be reliably detected in a 20 ppb O_3 background. However, if the recovery/exposure time were longer, the detection of NO_2 in higher O_3 backgrounds may be possible.

The start plot (left panel in figure 4.13), shows the peak position at the beginning of the NO_2 exposures, when subjected to 20,40 and 80 ppb O_3 backgrounds. Between 20 and 40 ppb, the start value does increase, this is expected, as increased concentrations lead to higher peak shifts (from figure 4.4). A further increase of 0.3 nm, would be expected for 80 ppb as well, however, a decrease in the start is observed instead, with the averaged start value being $\approx$ 834.5 nm. This could be

due to the NO_2 having an effect on the surface, but it is most likely caused by a too short recovery time before the O_3 background is introduced.

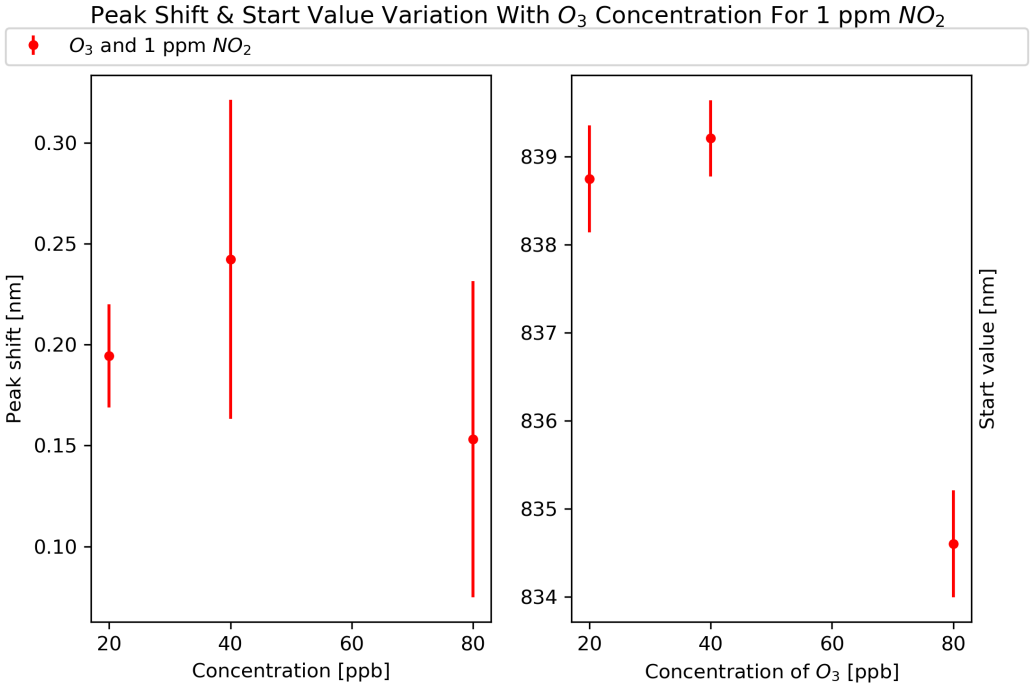

Figure 4.13: Peak shift variation for 20,40,80 ppb of O_3 background with 1 ppm NO_2 cycles.

5

Conclusion

In conclusion, a suitable temperature of operation for NO_2 sensing is 200 °C, while O_3 responds best at 300 °C. Increasing the reactor temperature does improve kinetics, however, it leads to instability from the increased thermal energy in the system, increasing the probability of desorption. A balance must therefore be found between speed and accuracy.

At the temperature of 250°C, a clearly increasing trend of peak shift with concentration is visible above 20 ppb NO_2. A similar trend is apparent for O_3, showing a steeper gradient.

The sensor is highly responsive to O_3, with peak shifts at 100 ppb O_3 of ≈2 nm, compared to ≈0.4 nm for 100 ppb NO_2. O_3 exposures show faster kinetics compared to NO_2, with a plateau in the peak position plot reached after 15 minutes.

Up to 20 ppb of O_3 background, the sensor can be effectively used to detect 1 ppm NO_2, given a 2 hour exposure and 2 hour recovery time. For 40 ppb and 80 ppb of O_3 background, instability in the behaviour of the sensor becomes apparent, as well as drift. A sensor shielding solution would potentially be required. The detecting of NO_2 may be possible above 20 ppb O_3 background, if allowed a longer exposure/recovery time.

If further study were to be conducted. A first step would be to recreate the experiments performed in this study, with special attention to the sensor having achieved complete saturation/recovery.

A mathematical way of predicting the saturation peak shift would be of interest, a first attempt is presented in appendix B. Through this treatment, the extraction of physical parameters such as a rate constant for the adsorption process could potentially be determined.

Additionally, exploring the option of different coatings or conducting an experiment with a constant NO_2 background and O_3 exposures is another suggestion for further work.

Bibliography

[1] R. P. Feynman, "There's plenty of room at the bottom", California Institute of Technology, Engineering and Science magazine (1960).

[2] P. Colomban, "The use of metal nanoparticles to produce yellow, red and iridescent colour, from bronze age to present times in lustre pottery and glass: solid state chemistry, spectroscopy and nanostructure", in Journal of nano research, Vol. 8 (Trans Tech Publ, 2009), pp. 109–132.

[3] A. Dmitriev, *Nanoplasmonic sensors* (Springer Science & Business Media, 2012).

[4] A. Mirzaei, K. Janghorban, B. Hashemi, and G. Neri, "Metal-core@ metal oxide-shell nanomaterials for gas-sensing applications: a review", Journal of Nanoparticle Research **17**, 371 (2015).

[5] K. Wetchakun, T. Samerjai, N. Tamaekong, C. Liewhiran, C. Siriwong, V. Kruefu, A. Wisitsoraat, A. Tuantranont, and S. Phanichphant, "Semiconducting metal oxides as sensors for environmentally hazardous gases", Sensors and Actuators B: Chemical **160**, 580–591 (2011).

[6] R. Vingarzan, "A review of surface ozone background levels and trends", Atmospheric environment **38**, 3431–3442 (2004).

[7] D. Nuvolone, D. Petri, and F. Voller, "The effects of ozone on human health", Environmental Science and Pollution Research **25**, 8074–8088 (2018).

[8] P. Hofmann, *Solid state physics: an introduction* (John Wiley & Sons, 2015).

[9] E. Martinsson, "Nanoplasmonic sensing using metal nanoparticles", PhD thesis (Linköping University Electronic Press, 2014).

[10] L. Saadi, C. Lambert-Mauriat, V. Oison, H. Ouali, and R. Hayn, "Mechanism of nox sensing on wo3 surface: first principle calculations", Applied surface science **293**, 76–79 (2014).

[11] J. M. Berak and M. Sienko, "Effect of oxygen-deficiency on electrical transport properties of tungsten trioxide crystals", Journal of Solid State Chemistry **2**, 109–133 (1970).

[12] M. Gillet, C. Lemire, E. Gillet, and K. Aguir, "The role of surface oxygen vacancies upon wo3 conductivity", Surface Science **532**, 519–525 (2003).

[13] W. Fang, Y. Yang, H. Yu, X. Dong, T. Wang, J. Wang, Z. Liu, B. Zhao, and M. Yang, "One-step synthesis of flower-shaped wo 3 nanostructures for a high-sensitivity room-temperature no x gas sensor", RSC advances **6**, 106880–106886 (2016).

[14] D. E. Williams, S. R. Aliwell, K. F. Pratt, D. J. Caruana, R. L. Jones, R. A. Cox, G. M. Hansford, and J. Halsall, "Modelling the response of a tungsten oxide semiconductor as a gas sensor for the measurement of ozone", Measurement Science and Technology **13**, 923 (2002).

[15] J. Guérin, K. Aguir, M. Bendahan, and C. Lambert-Mauriat, "Thermal modelling of a wo3 ozone sensor response", Sensors and Actuators B: Chemical **104**, 289–293 (2005).

[16] K. Aguir, C. Lemire, and D. Lollman, "Electrical properties of reactively sputtered wo3 thin films as ozone gas sensor", Sensors and actuators B: Chemical **84**, 1–5 (2002).

[17] V. Oison, L. Saadi, C. Lambert-Mauriat, and R. Hayn, "Mechanism of co and o3 sensing on wo3 surfaces: first principle study", Sensors and Actuators B: Chemical **160**, 505–510 (2011).

[18] H. Fredriksson, Y. Alaverdyan, A. Dmitriev, C. Langhammer, D. S. Sutherland, M. Zäch, and B. Kasemo, "Hole–mask colloidal lithography", Advanced Materials **19**, 4297–4302 (2007).

[19] P. J. Kelly and R. D. Arnell, "Magnetron sputtering: a review of recent developments and applications", Vacuum **56**, 159–172 (2000).

[20] O. Berger, T. Hoffmann, W.-J. Fischer, and V. Melev, "Tungsten-oxide thin films as novel materials with high sensitivity and selectivity to no 2, o 3, and h 2 s. part ii: application as gas sensors", Journal of Materials Science: Materials in Electronics **15**, 483–493 (2004).

A

Appendix 1

A.1 Details on Data Processing

An important step in the data processing was separating out the exposures. instances when the gas of interest is injected into the system. In the computer programme, whenever the flow rate of the gas of interest is present, the peak shift data is isolated and stored in a separate file. Allowing the treatment of each exposure individually. In figure A.1, the separated exposures are denoted in different colours.

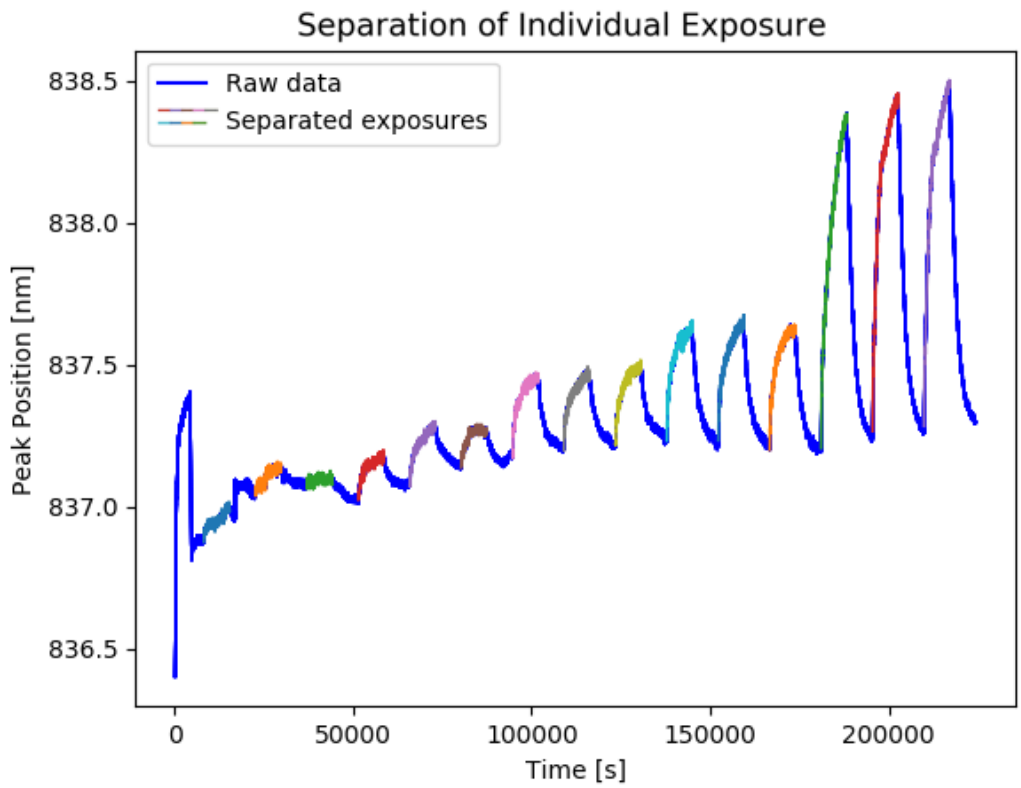

Figure A.1: Separation of each exposure, each colour represents a different measurement instance

A.2 Fitting equation

The response of the sensors can be fitted using a Langmuir isotherm [20]. In the referenced research, equation A.1, is used to predict the response of resistive sensors.

$$C = C_{s\infty}[1 - (1 - B)\exp^{-t/\tau_1} - B\exp^{-t/\tau_2}] \tag{A.1}$$

$C_{s\infty}$ is the dimensionless gas concentration on the surface of the WO_3 film. This is an analytical solution with details given in [20]. τ_1,τ_2 correspond to the rate constant from a probability that the species is adsorbed and contributions from bulk diffusion of the gas into the subsurface of WO_3 the film respectively [20]. Using this equation was attempted, however through trial and error the following modified equation was used (equation A.1)

The fitting equation A.2 was elaborated to explore whether the future behaviour of the exposures can be predicted. This equation is only present in a mathematical sense as any physical parameters cannot be conclusively determined to apply to the nanoplasmonic system used here.

$$\lambda_p = \lambda_s + \delta\lambda_{s\infty}[1 - (1 - B)\exp^{-t/\tau_1} - B\exp^{-t/\tau_2}] \tag{A.2}$$

With λ_p being the peak position at saturation. λ_s the wavelength at the beginning of the exposure to gas and $\delta\lambda$ the maximal peak shift. τ_1 and τ_2 are purely mathematical parameters.

B

Appendix 2

B.1 Convergence test: Predicting saturation

As a first step, it is useful to explore how quickly the function can be used to obtain the final peak shift. This is presented in figure B.1. This peak is peak 7, from figure 4.11.

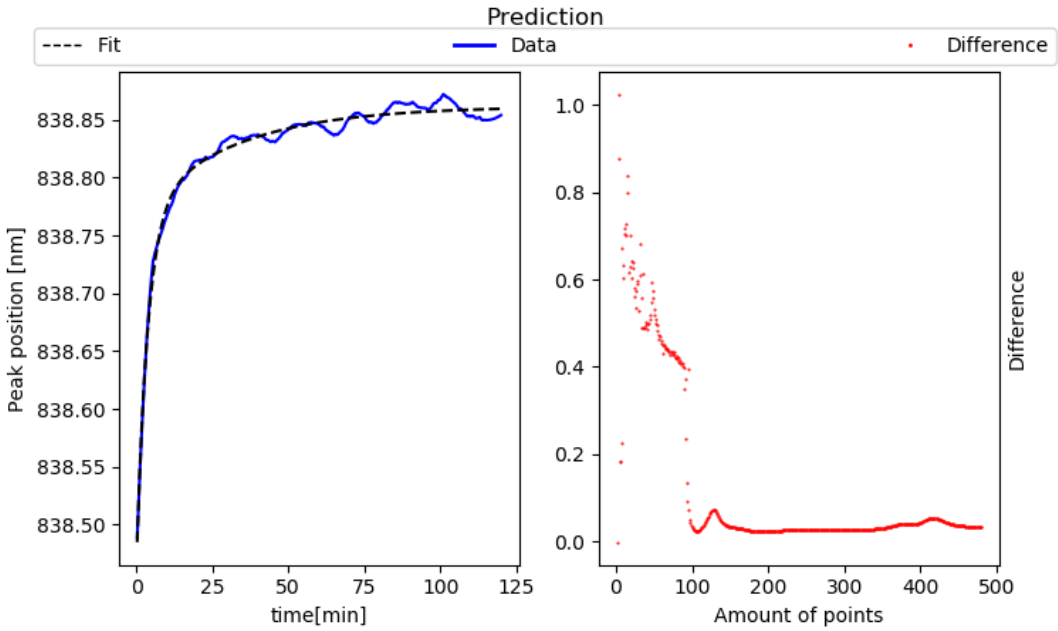

Figure B.1: Convergence test, raw data and fitted function on the left, comparison of difference between predicted peak shift and peak shift prediction with the given amount of points on the right.

As can be seen, the curve has reached sustained saturation after approximately 25 minutes. The difference between the predicted peak shift and actual peak shift, stabilises and varies little after 100 points, i.e 25 minutes. According to this basic analysis, the fit can be trusted to fit well, however as it varies strongly before the saturation, its reliability can be questioned.

C

Appendix 3

C.1 O_3 and NO_2 Temperature Sweep

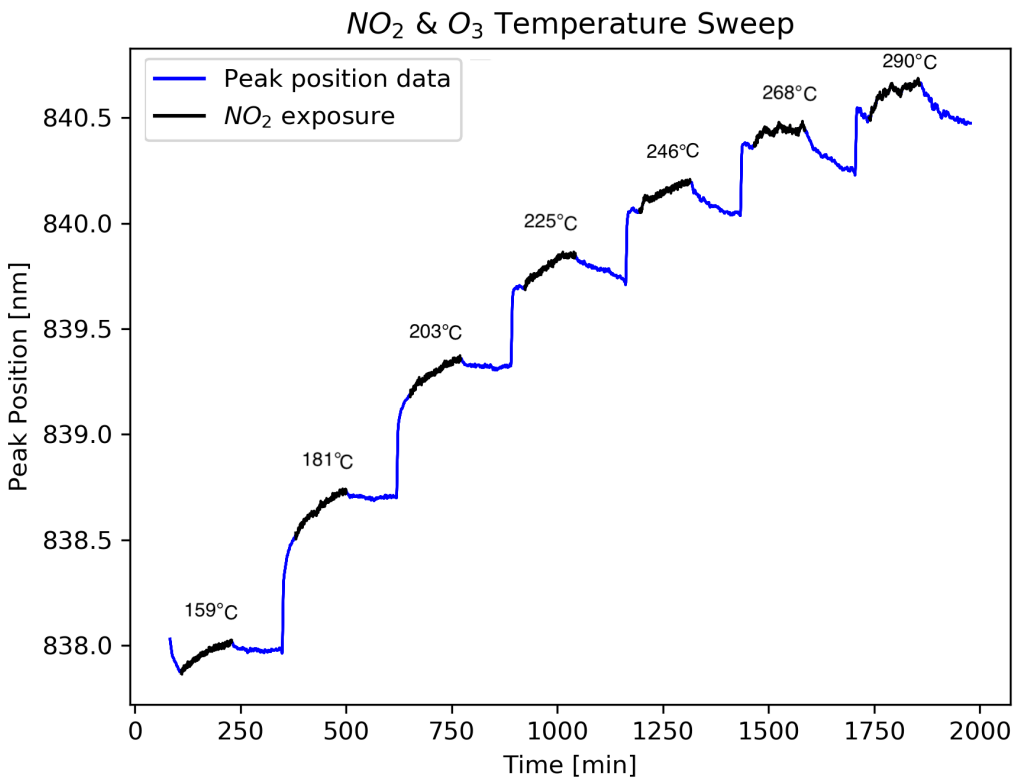

Figure C.1: NO_2 and O_3 temperature sweep in steps of 20°, 1 ppm NO_2, 40 ppb O_3 background.

A temperature sweep from 160°C to 280°C in steps of 20°C can be seen in figure C.1. Compared to the separate temperature sweeps, all the peaks appear to be very shallow. This can be explained by the fact that at high temperatures, despite the fact that desorption affects both O_3 and NO_2, O_3 is more present on the surface, poisoning the sensor.

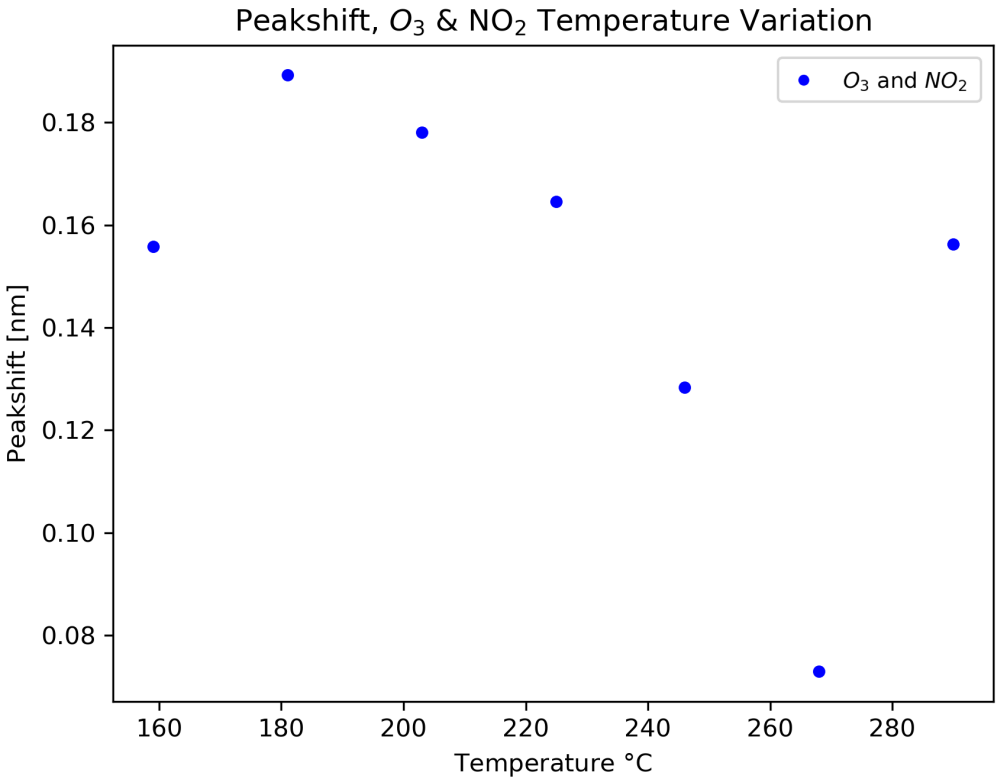

Figure C.2: Comparison of fit parameters for different temperatures, NO_2 in conjunction with 50 ppb O_3 background.

The data in figure C.2 shows a general decrease. The curve follows a similar shape to the one observed for NO_2. However, the maximum appears at 185°C.